# Bio-Inspired Fabrication of Hierarchical FeOOH Nanostructure Array Films at the Air−Water Interface, Their Hydrophobicity and Application for Water Treatment

Lei Liu, Liu-Qing Yang, Hai-Wei Liang, Huai-Ping Cong, Jun Jiang, and Shu-Hong Yu*

Division of Nanomaterials & Chemistry, Hefei National Laboratory for Physical Sciences at Microscale, Department of Chemistry,CAS Key Laboratory of Mechanical Behavior and Design of Materials, the National Synchrotron Radiation Laboratory, University of Science and Technology of China, Hefei 230026, P. R. China

ABSTRACT Hierarchical FeOOH nanostructure array films constructed by different nanosized building blocks can be synthesized at the air−water interface *via* a bio-inspired gas−liquid diffusion method. In this approach, poly(acrylic acid) (PAA) as a crystal growth modifier plays a crucial role in mediating the morphology and polymorph of FeOOH crystals. With the increase of PAA concentration, the shape of the building blocks assembling into FeOOH films can be tailored from nanosheets, to rice spikes, then to branched fibers, and finally to nanowires. What is more, a low concentration of PAA will induce the formation of α-FeOOH, while a high one could stabilize FeOOH in the form of the γ-FeOOH phase. After being modified with a thin layer of polydimethylsiloxane (PDMS), the as-prepared FeOOH films exhibited strong hydrophobicity with water contact angles (CA) from 134° to 148° or even superhydrophobicity with a CA of 164° in the sample constructed by nanosheets. When the FeOOH nanostructures were dispersed in water by ultrasound, they displayed quite promising adsorption performance of heavy metal ions for water treatment, where the highest adsorption capacity can reach 77.2 mg · g^{-1} in the sample constructed by nanowires. This bio-inspired approach may open up the possibilities for the fabrication of other functional nanostructure thin films with unique properties.
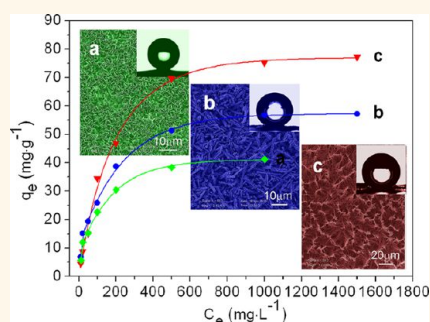
KEYWORDS: FeOOH · bio-inspired mineralization · hierarchical · array film · superhydrophobicity · water treatment

During the past several decades, a great deal of biominerals occurring in organisms have been confirmed to have three-dimensional ordered and hierarchical superstructures organized by nanosized building blocks with the control of biopolymers under ambient conditions.[1] Inspired by the formation process of biominerals, which is considered to take place through a bottom-up pathway, morphological control and nanostructural mediation of several inorganic materials in aqueous systems have been realized by bio-inspired mineralization strategies.[2,3] A large variety of novel and subtle morphologies and assemblies have been demonstrated, such as monodisperse spheres,[4] helices,[5,6] mesocrystals,[7,8] fibers,[9,10] complicated single crystals,[11−13] layered and multilayered structures,[14,15] and hierarchical architectures.[16,17]

However, these studies are mainly focused on alkaline earth metal-based carbonates.[18] Thus, expanding the bio-inspired mineralization approach to the design and preparation of nonbiological minerals is of great interest from the viewpoint of not only synthetic methodology but also practical applications.

Recently, some pioneering research on the synthesis of a few functional materials or their precursors employing a bio-inspired mineralization method has been reported. High crystalline α-Co(OH)$_2$ nanosheets and their oriented thin films can be selectively produced through the cooperation of spin-coated organic matrices and poly(acrylic acid) (PAA).[19] Calcite-type MnCO$_3$ crystals with ordered architecture were first produced in an organic gel matrix, which can be transformed into porous frameworks with connected LiMn$_2$O$_4$ nanoparticles, an

alternative cathode material for lithium-ion batteries, through a two-step calcination process *via* an intermediate of Mn_2O_3.[20] If the precursor solution contained both Co^{2+} and Mn^{2+} with a certain stoichiometric ratio, the final cobalt-doped $LiMn_2O_4$ system demonstrated improved cycle performance.[21] Highly porous $NiCo_2O_4$ sea urchin-like structures could also be obtained form the precursor of Ni−Co carbonate hydroxide, and these spinel structures displayed excellent supercapacitor performance and portend their applications in energy storage.[22]

Iron oxide-hydroxide (FeOOH), which occurs naturally as both geological[23] and biological[24] minerals, has three commonly found polymorphs: goethite (α-FeOOH), akaganeite (β-FeOOH), and lepidocrocite (γ-FeOOH).[25] FeOOH minerals are often used as precursors to produce Fe_2O_3 crystals with preserved shapes and nanostructures.[26,27] A promising application of this abundant and nontoxic mineral, which has a high affinity and large capacity for heavy metals,[33] for removal of heavy metal ions from a water system has been extensively studied in recent years.[28−32] However, these studies mainly concentrated on the following three aspects:[30] (i) modeling of the adsorption behavior demonstrated in experimental adsorption edges and isotherms;[33−35] (ii) direct spectroscopic investigation of the metal-mineral association;[36−38] (iii) influences on the removal capacity displayed by organic molecules[39,40] and inorganic ions.[41] There are few reports on exploring the effects of FeOOH morphology and polymorph on their water treatment performance.[42,43] What is more, although control over the sizes, shapes, and phases of FeOOH and other iron oxides-based nanocrystals has been widely explored and realized,[44−48] the presences of templates, surfactants, and toxic organic compounds involved in their synthesis process draw back their practical applications to some certain extent. Therefore, there is an urgent need to develop a mild, facile, and environmentally benign approach to prepare FeOOH minerals with specific morphologies, polymorphs, and micro/nanostructures that will endow them with larger scale applications in water treatment and other uses.

Herein, we demonstrate that FeOOH array films composed of various nanosized building blocks with different shapes can be produced at the air−water interface *via* a bio-inspired gas−liquid diffusion route. PAA as a crystal growth modifier plays an important role in mediating the morphology and polymorph of FeOOH minerals. As a whole, the array films exhibit different wettability from hydrophobicity (samples comprising nanowires, branched fibers, and rice spikes) to superhydrophobicity (sample comprising nanosheets). After ultrasonic dispersion in water, the samples are used for water treatment and the results demonstrate excellent performance for toxic heavy metal removal from aqueous solutions.
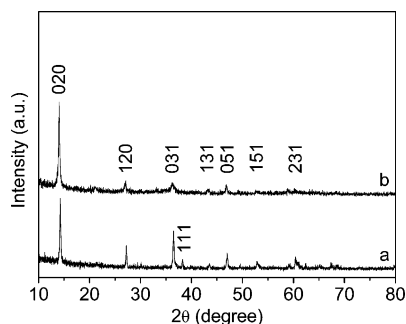

Figure 1. XRD patterns of FeOOH samples formed at air−water interface without (a) and with (b) the presence of PAA in bulk solution. Incubation time is 3 days. [$FeSO_4 \cdot 7H_2O$] = 20 mM, [PAA] = 0.6 g·L^{-1}.

RESULTS AND DISCUSSION

The polymorphs of the as-prepared product formed at the air−water interface were examined by XRD analysis (Figure 1). The sharp diffraction peaks in the XRD patterns implied that the samples had good crystallinity. The XRD patterns showed that all samples obtained with and without the presence of PAA in bulk solution were orthorhombic lepidocrocite (γ-FeOOH) with cell constants a = 3.87 Å, b = 12.4 Å, and c = 3.06 Å (JCPDS card 76-2301). Besides, it can be concluded from the XRD patterns that the use of PAA induced the increase of the relative intensity of γ-FeOOH {020} faces (Figure 1b), which would be attributed to the more exposure of these faces.

It cannot be determined only by XRD patterns whether there existed goethite (α-FeOOH) in the final product, because the diffraction peaks of goethite may possibly be covered by those of lepidocrocite. A trace of goethite can be clearly detected by FT-IR spectra (see Supporting Information, Figure S1). The absorption peaks at about 3410, 3130, and 2850 cm^{-1} belong to the stretching vibration of O−H.[49] The characteristic Fe−O−H bending vibration modes of γ-FeOOH can be clearly seen in the two spectra at about 1160 (in-plane), 1020 (in-plane), and 745 cm^{-1} (out-of-plane),[50] confirming the formation of γ-FeOOH in both cases. A trace of goethite was detected as revealed by the bands at 886 and 797 cm^{-1} which were assigned to in-plane and out-of-plane Fe−O−H bending vibrations of α-FeOOH, respectively.[23]

The typical scanning electron microscopy (SEM) and transmission electron microscopy (TEM) images of γ-FeOOH film structures produced without the control of PAA were shown in Figure 2a−c. It can be seen from the low-magnification SEM image (Figure 2a) that the film consisted of a large amount of highly ordered nanosheets (nearly) perpendicular to the air−water interface (film plane). While both sides (face-to-air and face-to-bulk solution) of the as-synthesized film displayed abundant sheet building blocks (inset in Figure 2a), the middle part was composed of a great deal of nanoparticles which stacked tightly to each
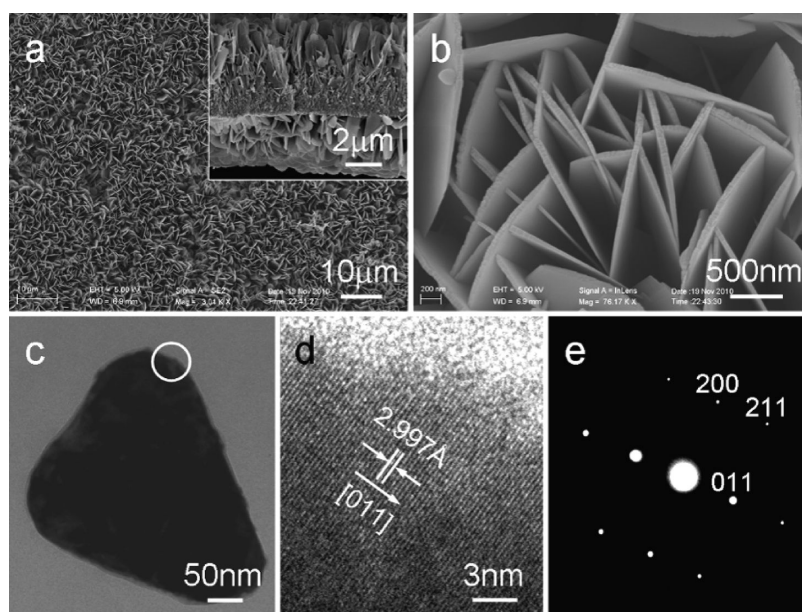
Figure 2. SEM (a, b) and TEM (c) images of γ-FeOOH nanosheets formed at the air−water interface. Corresponding HRTEM (d) and SAED pattern (e) of the part marked with white circle in panel c. Inset in panel a is cross-section view. Incubation time is 3 days. [FeSO$_4 \cdot$7H$_2$O] = 20 mM, [PAA] = 0.
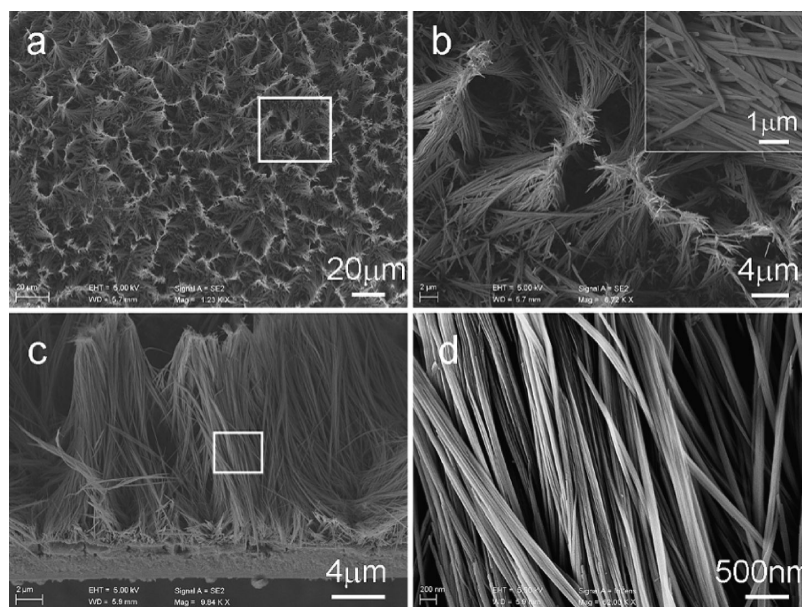

Figure 3. SEM images of γ-FeOOH nanowire array film formed at the air−water interface. (a, b) top view; (c, d) cross-section view; (b, d) enlarged images of the part marked with white squares in panel a and c, respectively. Incubation time is 3 days. [FeSO$_4 \cdot$7H$_2$O] = 20 mM, [PAA] = 0.6 g$\cdot$L^{-1}.

other as shown in the inset of Figure 2a. Figure 2b presented a high-magnification SEM image of γ-FeOOH nanosheets. The sheets with a thickness range of 30−70 nm had quite smooth surfaces. Similar structures have been reported for other systems such as NiO,[51] WO$_3$,[52] Cu$_{2-x}$Se,[53] and layered double hydroxide (LDH).[54,55] However, these array films were synthesized on solid substrates instead of air−water interface. More detailed information about a single nanosheet can be further provided by TEM, high resolution TEM (HRTEM) and selected area electron diffraction (SAED)

analyses. The clear SAED pattern (Figure 2e) can be indexed as γ-FeOOH, and the value of the lattice spacing of 3.00 Å measured from HRTEM image (Figure 2d) was consistent with that of (011) interplane spacing of γ-FeOOH. Furthermore, the HRTEM image and SAED pattern opened out the good crystallinity and monocrystalline nature of a single γ-FeOOH nanosheet.

SEM images in Figure 3 show that the building blocks of γ-FeOOH films obtained under the control of PAA (0.6 g$\cdot$L^{-1}) displayed a nanowire morphology,
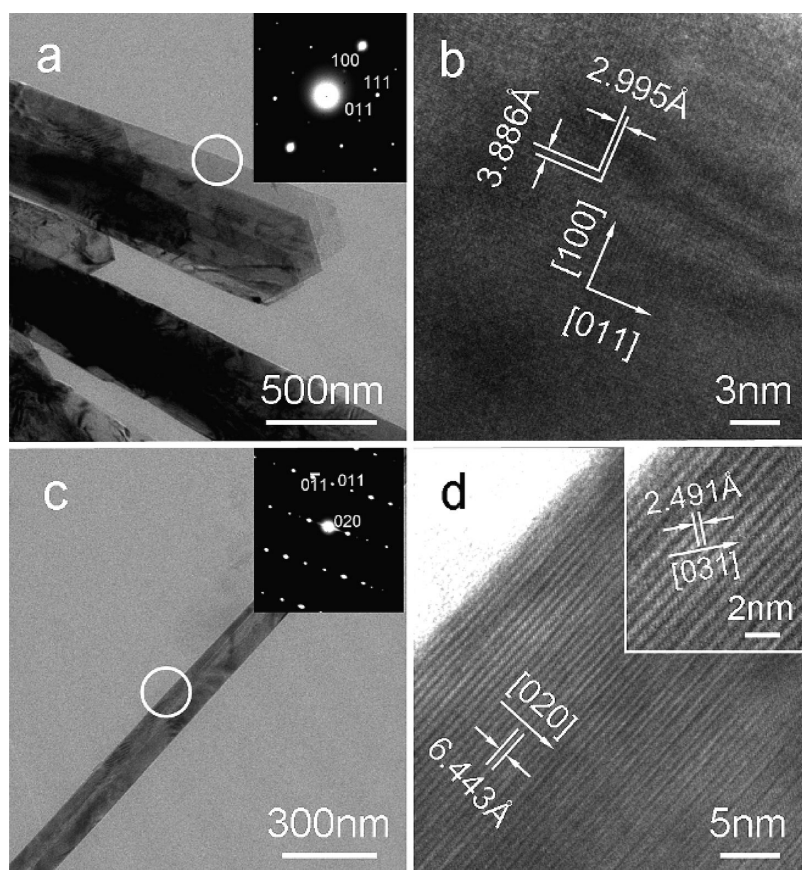
Figure 4. TEM and HRTEM images and corresponding SAED patterns of γ-FeOOH laths (a−c) and wires (d−f) formed at air−water interface under the control of PAA. Incubation time is 3 days. [FeSO$_4$·7H$_2$O] = 20 mM, [PAA] = 0.6 g·L^{-1}.

which was nearly perpendicular to the film plane. The tips of those adjacent nanowires congregate together with each other into clusters (Figure 3a,b), which may be caused by evaporation of water.[56] The shape of lepidocrocite building blocks (usually short ones) located near the bottom was closer to that of a lath other than a wire (inset in Figure 3b) which can be further confirmed by TEM image as shown in Figure 4a. From the cross-section SEM image (Figure 3c), it can be calculated that the wires have a typical length of about 15 μm, which can also be considered as the thickness of the nanowire array film in the present case. Clearly shown in enlarged SEM images (Figure 3d and Supporting Information, Figure S2), individual γ-FeOOH nanowires were further constructed or assembled from vast thinner fibrous nanosized building blocks. Also, similar nanowire array structures deposited on solid substrates have been found in several other inorganic systems as recently reviewed by Zhang and Yang.[57]

The detailed structures of a single nanolath or nanowire were further analyzed by TEM, HRTEM, and SAED as shown in Figure 4. Both of the two nanostructures had good crystallinity as confirmed by their HRTEM images (Figure 4b,d) and SAED patterns (insets in Figure 4a,c). Those relatively short γ-FeOOH laths with

a typical width of 430 nm overlapped with each other as shown in Figure 4a. Interplanar spacings of 3.886 Å and 2.995 Å measured in the HRTEM image of a single lath (Figure 4b) corresponded to the (100) and (011) crystalline planes of γ-FeOOH. The growth habit of γ-FeOOH laths obtained under the control of PAA was similar with that of those nanosheets formed in the absence of PAA (Figure 2). The only difference between the two structures was that the laths were elongated along the [011] direction. Single γ-FeOOH nanowire building blocks were also collected and examined by TEM, HRTEM, and SAED (Figure 4c,d). A single wire had an average diameter of about 120 nm and grew along the [001] direction of γ-FeOOH. The lattice spacings of 6.443 Å and 2.491 Å were consistent with (020) and (031) crystalline planes of γ-FeOOH, respectively, and the SAED taken from the white circle of the nanowire shown in the inset of Figure 4c was recorded from the [100] zone axis. The SAED pattern validated the monocrystalline nature of the observed γ-FeOOH nanowires as well.

According to the discussions described above, the morphology and microstructure of the as-synthesized FeOOH product were changed dramatically by adding PAA into FeSO$_4$ bulk solution. Thus, a series of experiments with different PAA contents in solution were

carried out to investigate the influence of PAA imposed on the changes of polymorphs and morphologies of final FeOOH crystals. The XRD patterns of the as-prepared samples obtained with different PAA concentrations were displayed in Figure 5. It can be observed that almost pure goethite was prepared under low PAA concentration (0.05 g·L^{-1}) as shown in Figure 5a. However, increasing the amount of PAA resulted in mixtures of goethite and lepidocrocite as indicated from the diffraction peaks which can be indexed accordingly (Figure 5b,c). Lepidocrocite became dominant in the sample (which just contained a trace of goethite) when the concentration of PAA increased to 0.5 g·L^{-1} (Figure 5d). As the PAA concentration increased up to 0.6 g·L^{-1}, lepidocrocite became the only phase in the final product (Figure 1b). The phase change of FeOOH arrays from almost pure goethite to a mixture of goethite and lepidocrocite, and finally to pure lepidocrocite, can be nicely captured by the choice of a suitable PAA content in FeSO$_4$ solution.

While the phases of the as-prepared FeOOH samples tightly depended on the concentration of PAA (Figure 5), the morphologies and configurations of
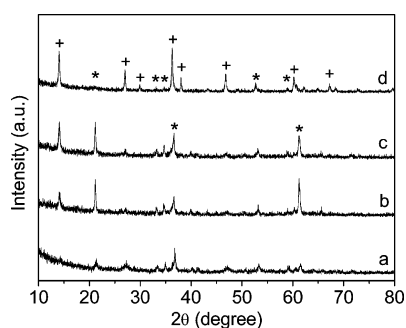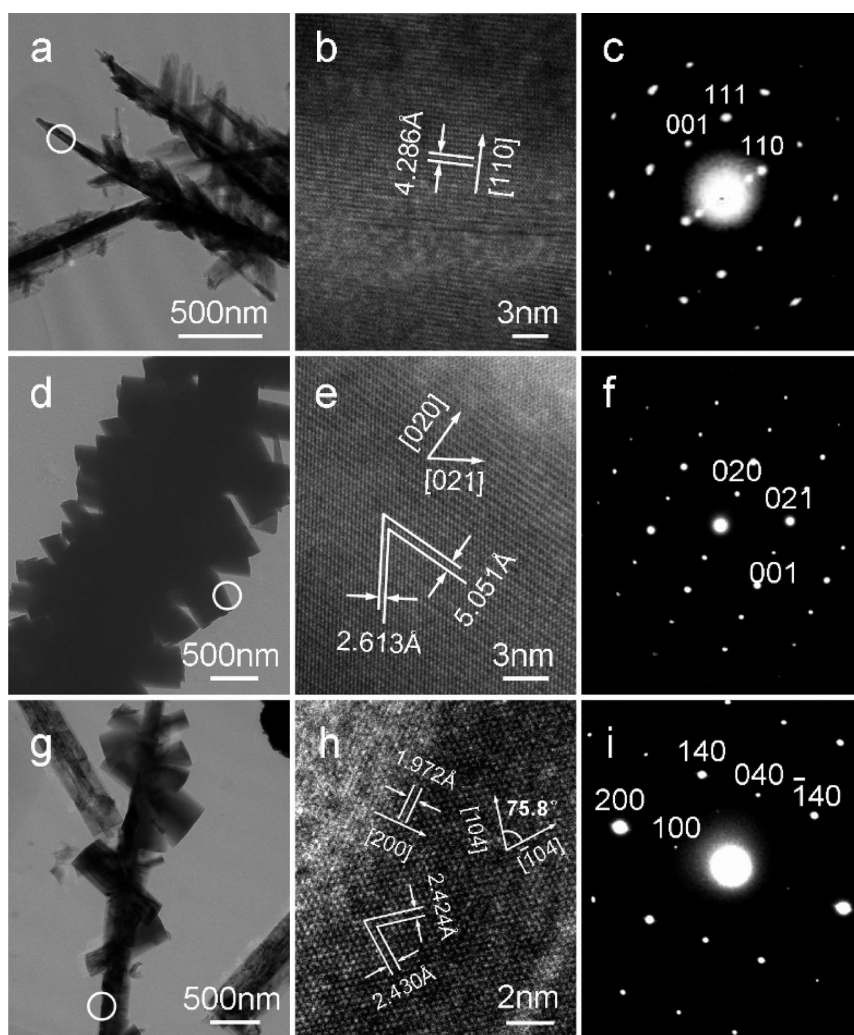

Figure 5. XRD patterns of FeOOH samples formed at the air−water interface with different PAA concentrations in bulk solution. (a) 0.05; (b) 0.1; (c) 0.2; (d) 0.5 g·L^{-1}. Incubation time is 3 days. [FeSO$_4$·7H$_2$O] = 20 mM. (+) phase of γ-FeOOH (JCPDS Card No. 76-2301); (∗) phase of α-FeOOH (JCPDS Card No. 81-0462).

these products can also be dramatically affected by PAA content as shown in Figure 6. Interestingly, it can be found that even a small amount of PAA (0.05 g·L^{-1}) in FeSO$_4$ solution will lead to remarkable differences in the morphologies of the nanosized building blocks changing from nanosheets (without PAA, Figure 2) to rice spikes (Figure 6a,e). These rice spikes stand perpendicular to the film plane and close to each other given the formation of FeOOH forest with high density (Figure 6a). From the enlarged SEM image (Figure 6e), several fibrous backbones grew from one site with a great deal of nanoflakes located on each backbone (Figure 6e and Supporting Information, Figure S3). Increasing PAA concentration resulted in chaotic accumulations of branched fibers as shown in Figure 6b,c. Compared with rice spikes in Figure 6e, the backbones of branched fibers were separated with each other (Figure 6f,g) instead of aggregated together. What is more, with the increase of PAA concentration in solution, the size and the number of branches grown from fibrous backbones increased and decreased, respectively (Figure 6e−g). At higher PAA concentration (0.5 g·L^{-1}), the branches disappeared and only some nanoparticles adhered to the surface of FeOOH wires (Figure 6d, h). Interestingly, it can be observed from a larger scale view that nanoparticle-decorated wires tilt almost along the same direction and made each wire located nearly parallel with one anther (see Supporting Information, Figure S4), which could be caused by directional water flow involved in their collection process. Besides, some hemeatite (α-Fe$_2$O$_3$) nanoparticles with irregular shape could deposit in FeSO$_4$ bulk solution and their morphology has no significant change by altering PAA concentration. While the nanoparticles obtained with low PAA concentration exhibit nearly spherical shape, those collected with high PAA concentration are closer to polyhedrons (see Supporting Information, Figure S5).

As described above, both the quantity of α-FeOOH in XRD patterns (Figure 5) and the number of branches
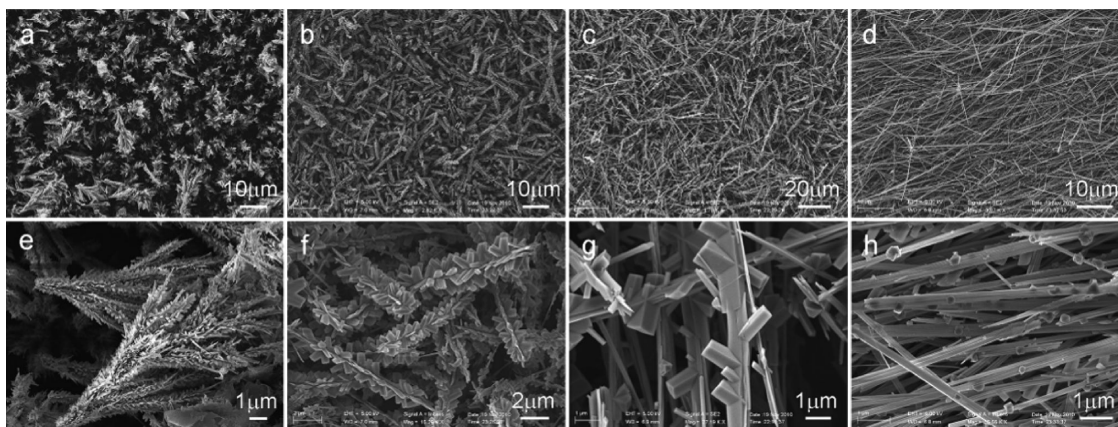
Figure 6. SEM images of FeOOH samples formed at the air−water interface with different PAA concentrations in bulk solution. (a,e) 0.05; (b, f) 0.1; (c,g) 0.2; (d,h) 0.5 g·L^{-1}. Incubation time is 3 days. [FeSO$_4$·7H$_2$O] = 20 mM.

Figure 7. TEM images, corresponding HR-TEM images and SAED patterns of FeOOH samples formed at the air−water interface with different PAA concentrations. (a−c): 0.05; (d−f): 0.1; (g−i): 0.2 g·L⁻¹. Incubation time is 3 days. [FeSO₄·7H₂O] = 20 mM.

on fibrous backbones (Figure 6e−h) decreased with the increase of PAA concentration. However, γ-FeOOH was boosted and the wire structures became more and more obvious at the same time. So it can be deduced that the backbones and the branches should correspond to the γ-FeOOH and α-FeOOH phases, respectively. To verify this hypothesis, TEM, HRTEM, and SAED analyses were further carried out (Figure 7).

From the detailed characterization of the rice spike sample obtained with low PAA content, it can be observed that even the backbones existed in the form of the α-FeOOH phase growing along the [001] direction (Figure 7a−c), which is in accordance with goethite crystal growth habit.[58] This is in good agreement with its XRD pattern (Figure 5a) where the characteristic diffraction peaks of γ-FeOOH are very weak. At intermediate PAA concentration, isolated branched fibers were produced with branches in goethite form which is confirmed by corresponding HRTEM and SAED results (Figure 7d−f and Supporting Information, Figure S6).

However, there were too many branches around isolated backbone fibers to identify the phase of centered backbones at [PAA] = 0.1 g·L⁻¹ (Figure 7d). As the PAA concentration was increased to 0.2 g·L⁻¹, the number of branches decreased obviously and part of the backbone fiber was exposed which could be examined. The HRTEM image and SAED spectrum shown in Figure 7 panels h and i verified their lepidocrocite nature. Clearly, all the results discussed can strongly support or consolidate our hypothesis proposed above.

The growth process of FeOOH array films at the air−water interface was followed by time-dependent experiments. The samples obtained without PAA and with relatively high PAA concentration (0.6 g·L⁻¹) were chosen as examples to study their formation mechanism. The transformation process of FeOOH structures can be clearly observed (Figure 8). At the early reaction stage (8 h), a layer of FeOOH nanoparticles can be observed for both samples (Figure 8a,d). When the incubation time is increased to 24 h, the
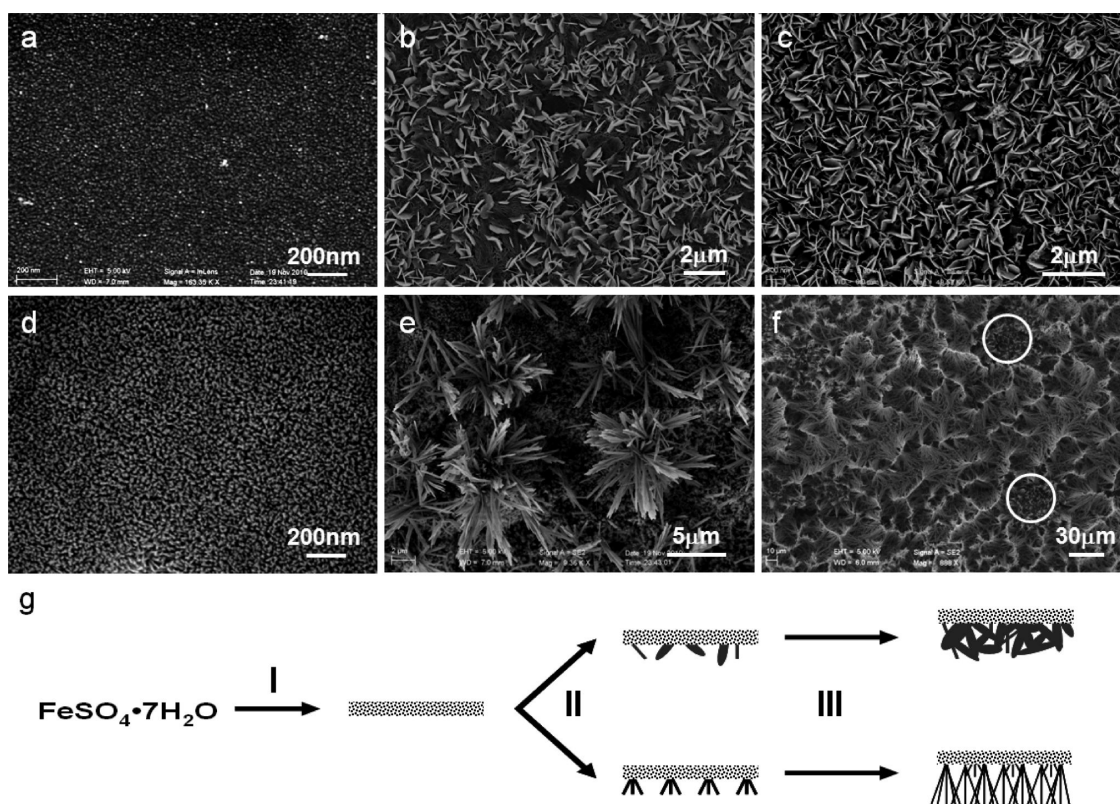
Figure 8. SEM images of FeOOH nanostructure films with different incubation times: (a,d) 8 h; (b,e) 24 h; (c,f) 48 h. (a−c) without PAA; (d−f) [PAA] = 0.6 g·L^{-1}; [FeSO$_4$·7H$_2$O] = 20 mM. (g) Schematic illustration of the formation process of FeOOH array films.

nanoparticle layers acted as growth substrates for isolated nanosheets without PAA (Figure 8b) and flower-like structures composed of nanowires with the control of PAA (Figure 8e). The surface of the nanoparticle layer was partly exposed in both cases. As the reaction proceeded, both the number and density of nanosheets increased and the surface of the nanoparticle layer could not be observed (Figure 8c, 48 h). For the sample mediated by PAA, as can be seen in Figure 8f, most of the nanoparticle layer surface was covered with grown nanowires and some of the flower-like structures can also be observed (white circles in Figure 8f and Supporting Information Figure S7). Well-defined FeOOH array films composed of nanosheets or nanowires were formed at the air−water interface after incubation for 3 days (Figure 2 and Figure 3).

On the basis of the above results of time-dependent experiments, a plausible growth mechanism of these FeOOH array films was proposed (Figure 8g). Initially, FeOOH nanoparticles stacked together forming a thin layer whether with or without the control of PAA. Subsequently, some isolated nanosheets and flower-like structures grew from FeOOH nanoparticle layer substrates without and with PAA mediation, respectively. As reaction continued, the number, size, and density of nanounits increased. After
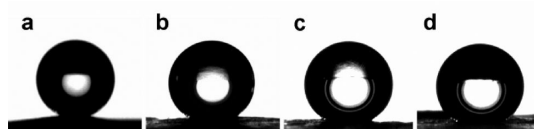

Figure 9. Optical graphs of the water drops on FeOOH films composed of different nanosized building blocks: (a) nanosheets, (b) rice spikes, (c) branched fibers, (d) wires.

prolonging incubation time, well-defined FeOOH array films composed of different nanounits can be prepared.

Self-cleaning surfaces inspired by the lotus leaf have attracted considerable attention and aroused much interest for their great advantages in practical applications.[59] There is a strong interaction between the wettability and the microstructure of materials surfaces. Large contact angle (CA) and small sliding angle (SA) can be realized on surfaces with homogeneous and well-organized micro/nanostructures.[60] The wettabilities of FeOOH array films with different subtle shapes and configurations in the present case were measured by means of water CA after these films were treated with polydimethylsiloxane (PDMS). The shapes of water droplets on different FeOOH films were displayed in Figure 9. The CA value measured on the surface of the film composed of nanosheets was 164°
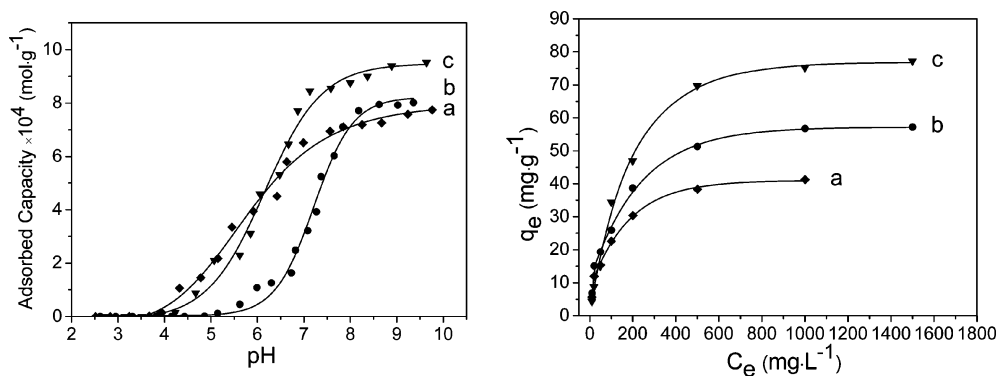
Figure 10. pH adsorption edges (left) and adsorption isotherms (right) of Cd^{2+} using sonicated FeOOH minerals with different morphologies: (a) nanosheets, (b) branched fibers, (c) wires.

(Figure 9a), which endows the sample with superhydrophobicity. However, for the samples of rice spikes and branched fibers, similar wettability was detected with a CA value of 143° and 148°, respectively (Figure 9b,c). The smallest CA value (134°) as shown in Figure 8d can be measured on the sample surface comprising nanowires, which maybe caused by vast distances of the nanowire clusters (Figure 3a).[61] The results discussed above demonstrate that films with strong hydrophobicity or even superhydrophobicity can be prepared in large scale through a facile and environmentally benign bio-inspired mineralization strategy and portend their potential applications as that of superhydrophobic surfaces.

A series of experiments have been performed by varying initial pH and concentration of Cd^{2+}, which is considered as a highly toxic pollutant in wastewater, to investigate the adsorption capacities of FeOOH minerals with different morphologies. The shapes of the pH adsorption edges of Cd^{2+} presented in the left panel in Figure 9 are in good agreement with previous studies.[30,62] The adsorption of Cd^{2+} on nanosheet and nanowire γ-FeOOH started above pH 4 (Figure 10, left panel a,c). However, this occurred with pH > 5 for a branched fiber sample (Figure 10, left panel b), which would be caused by the presence of α-FeOOH.[63]

The right panel in Figure 10 displays the adsorption isotherms of Cd^{2+} on three FeOOH samples, from which the adsorption capacities for Cd^{2+} of each FeOOH sample could be evaluated. The Langmuir adsorption model, $q_e = q_m b C_e/(1 + b C_e)$, is used to calculate the maximal adsorption capacity,[64] where q_e (mg·g^{-1}) and C_e (mg·L^{-1}) represent the amount of adsorbed heavy metal and the solute concentration at equilibrium; q_m (mg·g^{-1}) is the maximal adsorption capacity and b (L·mg^{-1}) is the equilibrium constant. The maximal adsorption capacities for Cd^{2+} of three FeOOH minerals with different morphologies are 41.7 mg·g^{-1} for nanosheets, 57.5 mg·g^{-1} for branched fibers, and 77.2 mg·g^{-1} for nanowires, respectively. All the values are much higher than those of other nanomaterials reported previously,

such as akaganeite nanocrystals (17.1 mg·g^{-1}),[65] P-25 nanoparticles (20.1 mg·g^{-1}),[66] and ETS-4 titanosilicate (24.7 mg·g^{-1}).[67]

Heavy metal ion adsorption on metal oxides is considered to be based on the combination of electrostatic attraction between charged oxides and ions, and ion exchange in aqueous solution.[42] In the present case, the subtle structures, nanoscale particle sizes, and relatively high BET surface areas (see Supporting Information, Figure S8) are beneficial for ion adsorption, exchange, diffusion, and thus the prominent adsorption performance. Besides, it is worth noting that the maximal adsorption capacities in this work were measured without any pH adjustment, which are different from those obtained at optimized pH values (usually about 2) in previous reports. We thus believe that the high adsorption capacities reported here are of higher practical application values in water treatment.

CONCLUSIONS

In summary, various FeOOH nanostructure array films have been synthesized at the air−water interface through a facile, mild, and environment-friendly bio-inspired gas−liquid diffusion method. PAA as a crystal growth modifier can exert significant influence on the morphologies and polymorphs of FeOOH mineral. With the increase of PAA concentration, the shape of the building blocks forming FeOOH films changed from nanosheets, to rice spikes, then to branched fibers, and finally to nanowires. What is more, the phase change of FeOOH crystals from almost pure α-FeOOH to mixtures of α-FeOOH and γ-FeOOH, and finally to pure γ-FeOOH can also be nicely captured by the choice of a suitable PAA concentration in precursor solutions. The results suggested that the backbones and branches in FeOOH samples corresponded to γ-FeOOH and α-FeOOH, respectively. Different morphologies of nanosized building blocks endowed the FeOOH films with diverse wettability from hydrophobicity to superhydrophobicity (nanosheet sample with CA of 164°). After being dispersed in water by

ultrasonic treatment, the FeOOH nanosized building blocks exhibit excellent water treatment performance with high adsorption capacities toward heavy metal ions, such as 77.2 mg·g^{-1} for γ-FeOOH nanowires, which are vastly superior to many other nanomaterials reported previously.[65−67]

MATERIALS AND METHOD

All chemical reagents are of analytical grade and used as received without further purification.

Preparation of FeOOH Arrays. The preparation of FeOOH arrays was carried out using a slow gas−liquid diffusion technique as described elsewhere.[19] In a typical synthesis, 40 mL of aqueous solution of FeSO$_4$·7H$_2$O with different PAA concentrations was poured into a glass beaker. Then three beakers were covered with parafilm, which were punched with four needle holes, and placed in a closed desiccator. Another three glass bottles filled with 10 mL of diluted NH$_4$OH solution (2.5 wt %) were also covered with parafilm, punched with four needle holes, and placed at the bottom of the desiccator. After a certain period of incubation time at room temperature, a brownish thin film was deposited at the air−water interface in each glass beaker. The film was transferred onto a clean glass substrate and dried at room temperature for further characterization.

Characterization. The final crystals were examined by X-ray powder diffraction (XRD), scanning electron microscopy (SEM), Fourier transform infrared (FT-IR), (high resolution) transmission electron microscopy ((HR-)TEM), selected area electron diffraction (SAED), and water contact angle (CA). XRD analyses were carried out on a Philips X'Pert PRO SUPER X-ray diffractometer equipped with graphite monochromatized Cu Kα radiation (λ = 1.54056 Å) and the operation voltage and current were maintained at 40 kV and 40 mA, respectively. SEM was performed on a Zeiss SUPRA 40 field emission microscope. FT-IR spectra were measured on a MAGNA-IR 750. TEM, HR-TEM, and SAED were performed on a JEOL JSM-2010F transmission electron microscope at 200 kV. CA measurement was carried out on OCA 40 optical contact angle meter at ambient conditions. Nitrogen adsorption was performed on an ASAP 2020 Accelerated Surface Area and Porosimetry (Micromeritics) at 77 K using Barrett−Emmett−Teller (BET) calculations for surface area.

Removal of Heavy Metal Ion. Cd^{2+} was used as an example to study the water treatment performance of FeOOH samples in the present case. Different FeOOH films were sonicated for 40 min in water to form a homogeneous dispersion (1 g·L^{-1}). The pH adsorption edge experiments with [Cd^{2+}] = 1 mM covered a pH range of 2−10, which was adjusted using 0.1 M HNO$_3$ and 0.1 M NaOH every 4 h. The ionic strength of the above solution, I, was adjusted to 0.1 M with NaNO$_3$. To obtain the adsorption isotherms for calculation of maximal adsorption capacity, various amounts of Cd(NO$_3$)$_2$ were added into FeOOH dispersions forming a series of solutions with different [Cd^{2+}] (10, 20, 50, 100, 200, 500, 1000, 1500 mg·L^{-1}) under stirring at room temperature. After being stirred for 12 h, the solid and liquid were separated by centrifugation and the concentration of Cd^{2+} was measured by inductively coupled plasma atomic emission spectroscopy (ICP-AES, Thermo Jarrell Ash, Atomscan Advantage).

Conflict of Interest: The authors declare no competing financial interest.

Supporting Information Available: FT-IR spectra, SEM, TEM, and HRTEM images, SAED pattern, and nitrogen sorption isotherm as described in the text. This material is available free of charge *via* the Internet at http://pubs.acs.org.

REFERENCES AND NOTES

1. Mayer, G. Rigid Biological Systems as Models for Synthetic Composites. *Science* **2005**, *310*, 1144–1147.
2. Yu, S. H. Bio-inspired Crystal Growth by Synthetic Templates. *Top. Curr. Chem.* **2007**, *271*, 79–118.
3. Chen, S. F.; Zhu, J. H.; Jiang, J.; Cai, G. B.; Yu, S. H. Polymer Controlled Crystallization of Unique Mineral Superstructures. *Adv. Mater.* **2010**, *22*, 540–545.
4. Guo, X. H.; Yu, S. H.; Cai, G. B. A New Controlled Crystallization Approach in a Mixed Solution Using an Artificial Peptide Type Block Copolymer as a Crystal Modifier: Highly Monodisperse CaCO$_3$ Microspheres and Morphology Control. *Angew. Chem., Int. Ed.* **2006**, *45*, 3977–3981.
5. Yu, S. H.; Cölfen, H.; Tauer, K.; Antonietti, M. Tectonic Arrangement of BaCO$_3$ Nanocrystals into Helices Induced by a Racemic Block Copolymer. *Nat. Mater.* **2005**, *4*, 51–55.
6. Zhu, J. H.; Yu, S. H.; Xu, A. W.; Cölfen, H. Biomimetic Mineralization of Double-Stranded and Cylindrical Helical BaCO$_3$ Nanofibres. *Chem. Commun.* **2009**, 1106–1108.
7. Wang, T. X.; Antonietti, M.; Cölfen, H. Calcite Mesocrystals: "Morphing" Crystals by a Polyelectrolyte. *Chem.—Eur. J.* **2006**, *12*, 5722–5730.
8. Geng, X.; Liu, L.; Jiang, J.; Yu, S. H. Crystallization of CaCO$_3$ Mesocrystals and Complex Aggregates in a Mixed Solvent Media Using Polystyrene Sulfonate as a Crystal Growth Modifier. *Cryst. Growth Des.* **2010**, *10*, 3448–3453.
9. Olszta, M. J.; Gajjeraman, S.; Kaufman, M.; Gower, L. B. Nanofibrous Calcite Synthesized *via* a Solution−Precursor−Solid Mechanism. *Chem. Mater.* **2004**, *16*, 2355–2362.
10. Zhu, J. H.; Song, J. M.; Yu, S. H.; Zhang, W. Q.; Shi, J. X. Mineralization for Micropatterned Growth of Carbonate Nanofibers. *CrystEngComm* **2009**, *11*, 539–541.
11. Park, R. J.; Meldrum, F. C. Synthesis of Single Crystals of Calcite with Complex Morphologies. *Adv. Mater.* **2002**, *14*, 1167–1169.
12. Li, C.; Qi, L. M. Bioinspired Fabrication of 3D Ordered Macroporous Single Crystals of Calcite from a Transient Amorphous Phase. *Angew. Chem., Int. Ed.* **2008**, *47*, 2388–2393.
13. Finnemore, A. S.; Scherer, M. R. J.; Langford, R.; Mahajan, S.; Ludwigs, S.; Meldrum, F. C.; Steiner, U. Nanostructured Calcite Single Crystals with Gyroid Morphologies. *Adv. Mater.* **2009**, *21*, 3928–3932.
14. Kato, T. Polymer/Calcium Carbonate Layered Thin-Film Composites. *Adv. Mater.* **2000**, *12*, 1543–1546.
15. Wei, H.; Ma, N.; Shi, F.; Wang, Z. Q.; Zhang, X. Artificial Nacre by Alternating Preparation of Layer-by-Layer Polymer Films and CaCO$_3$ Strata. *Chem. Mater.* **2007**, *19*, 1974–1978.
16. Oaki, Y.; Imai, H. The Hierarchical Architecture of Nacre and Its Mimetic Material. *Angew. Chem., Int. Ed.* **2005**, *4*, 6571–6575.
17. Oaki, Y.; Imai, H. Hierarchically Organized Superstructure Emerging from the Exquisite Association of Inorganic Crystals, Organic Polymers, and Dyes: A Model Approach Towards Suprabiomineral Materials. *Adv. Funct. Mater.* **2005**, *15*, 1407–1414.
18. Meldrum, F. C.; Cölfen, H. Controlling Mineral Morphologies and Structures in Biological and Synthetic Systems. *Chem. Rev.* **2008**, *108*, 4332–4432.

19. Oaki, Y.; Kajiyama, S.; Nishimura, T.; Kato, T. Selective Synthesis and Thin-Film Formation of α-Cobalt Hydroxide through an Approach Inspired by Biomineralization. *J. Mater. Chem.* **2008**, *18*, 4140–4142.

20. Uchiyama, H.; Hosono, E.; Zhou, H.; Imai, H. Three-Dimensional Architectures of Spinel-Type LiMn$_2$O$_4$ Prepared from Biomimetic Porous Carbonates and Their Application to a Cathode for Lithium-Ion Batteries. *J. Mater. Chem.* **2009**, *19*, 4012–4016.

21. Kokubu, T.; Oaki, Y.; Uchiyama, H.; Hosono, E.; Zhou, H.; Imai, H. Biomimetic Synthesis of Metal Ion-Doped Hierarchical Crystals Using a Gel Matrix: Formation of Cobalt-Doped LiMn$_2$O$_4$ *via* Cobalt-Doped MnCO$_3$ Precursor and the Improved Electrochemical Properties. *Chem. Asian J.* **2010**, *5*, 792–798.

22. Xiao, J. W.; Yang, S. H. Sequential Crystallization of Sea Urchin-like Bimetallic (Ni, Co) Carbonate Hydroxide and Its Morphology Conserved Conversion to Porous NiCo$_2$O$_4$ Spinel for Pseudocapacitors. *RSC Adv.* **2011**, *1*, 588–595.

23. Chen, R. F.; Chen, H. X.; Wei, Y.; Hou, D. L. Photocatalytic Oxidation of Fe(OH)$_2$ Suspension with Visible Light Irradiation. *J. Phys. Chem. C* **2007**, *111*, 16453–16459.

24. Sone, E. D.; Weiner, S.; Addadi, L. Morphology of Goethite Crystals in Developing Limpet Teeth: Assessing Biological Control over Mineral Formation. *Cryst. Growth Des.* **2005**, *5*, 2131–2138.

25. Chaudhari, N. K.; Yu, J. S. Size Control Synthesis of Uniform β-FeOOH to High Coercive Field Porous Magnetic α-Fe$_2$O$_3$ Nanorods. *J. Phys. Chem. C* **2008**, *112*, 19957–19962.

26. Piao, Y.; Kim, J.; Na, H. B.; Kim, D.; Baek, J. S.; Ko, M. K.; Lee, J. H.; Shokouhimehr, M.; Hyeon, T. Wrap−Bake−Peel Process for Nanostructural Transformation from β-FeOOH Nanorods to Biocompatible Iron Oxide Nanocapsules. *Nat. Mater.* **2008**, *7*, 242–247.

27. Meng, F.; Morin, S. A.; Jin, S. Rational Solution Growth of α-FeOOH Nanowires Driven by Screw Dislocations and Their Conversion to α-Fe$_2$O$_3$ Nanowires. *J. Am. Chem. Soc.* **2011**, *133*, 8408–8411.

28. Farquhar, M. L.; Charnock, J. M.; Livens, F. R.; Vaughan, D. J. Mechanisms of Arsenic Uptake from Aqueous Solution by Interaction with Goethite, Lepidocrocite, Mackinawite, and Pyrite: an X-ray Absorption Spectroscopy Study. *Environ. Sci. Technol.* **2002**, *36*, 1757–1762.

29. Hanna, K.; Carteret, C. Sorption of 1-Hydroxy-2-Naphthoic Acid to Goethite, Lepidocrocite and Ferrihydrite: Batch Experiments and Infrared Study. *Chemosphere* **2007**, *70*, 178–186.

30. Peacock, C. L.; Sherman, D. M. Copper(II) Sorption onto Goethite, Hematite and Lepidocrocite: A Surface Complexation Model Based on *ab Initio* Molecular Geometries and EXAFS Spectroscopy. *Geochim. Cosmochim. AC.* **2004**, *68*, 2623–2637.

31. Buerge-Weirich, D.; Hari, R.; Xue, H. B.; Behra, P.; Sigg, L. Adsorption of Cu, Cd, and Ni on Goethite in the Presence of Natural Groundwater Ligands. *Environ. Sci. Technol.* **2002**, *36*, 328–336.

32. Leuz, A. K.; Monch, H.; Johnson, C. A. Sorption of Sb(III) and Sb(V) to Goethite: Influence on Sb(III) Oxidation and Mobilization. *Environ. Sci. Technol.* **2006**, *40*, 7277–7282.

33. Xu, Y.; Axe, L.; Yee, N.; Dyer, J. A. Bidentate Complexation Modeling of Heavy Metal Adsorption and Competition on Goethite. *Environ. Sci. Technol.* **2006**, *40*, 2213–2218.

34. Villalobos, M.; Trotz, M. A.; Leckie, J. O. Surface Complexation Modeling of Carbonate Effects on the Adsorption of Cr(VI), Pb(II), and U(VI) on Goethite. *Environ. Sci. Technol.* **2001**, *35*, 3849–3856.

35. Kanematsu, M.; Young, T. M.; Fukushi, K.; Green, P. G.; Darby, J. L. Extended Triple Layer Modeling of Arsenate and Phosphate Adsorption on a Goethite-Based Granular Porous Adsorbent. *Environ. Sci. Technol.* **2010**, *44*, 3388–3394.

36. Ona-Nguema, G.; Morin, G.; Juillot, F.; Calas, G.; Brown, G. E. EXAFS Analysis of Arsenite Adsorption onto Two-Line Ferrihydrite, Hematite, Goethite, and Lepidocrocite. *Environ. Sci. Technol.* **2005**, *39*, 9147–9155.

37. Beattie, D. A.; Chapelet, J. K.; Grafe, M.; Skinner, W. M.; Smith, E. *In Situ* ATR FTIR Studies of SO$_4$ Adsorption on Goethite in the Presence of Copper Ions. *Environ. Sci. Technol.* **2008**, *42*, 9191–9196.

38. Arai, Y. X-ray Absorption Spectroscopic Investigation of Molybdenum Multinuclear Sorption Mechanism at the Goethite−Water Interface. *Environ. Sci. Technol.* **2010**, *44*, 8491–8496.

39. Weng, L. P.; Van Riemsdijk, W. H.; Hiemstra, T. Effects of Fulvic and Humic Acids on Arsenate Adsorption to Goethite: Experiments and Modeling. *Environ. Sci. Technol.* **2009**, *43*, 7198–7204.

40. Marcussen, H.; Holm, P. E.; Strobel, B. W.; Hansen, H. C. B. Nickel Sorption to Goethite and Montmorillonite in Presence of Citrate. *Environ. Sci. Technol.* **2009**, *43*, 1122–1127.

41. Cheng, T.; Barnett, M. O.; Roden, E. E.; Zhuang, J. L. Effects of Phosphate on Uranium(VI) Adsorption to Goethite-Coated Sand. *Environ. Sci. Technol.* **2004**, *38*, 6059–6065.

42. Li, H.; Li, W.; Zhang, Y.; Wang, T.; Wang, B.; Xu, W.; Jiang, L.; Song, W.; Shu, C.; Wang, C. Chrysanthemum-like α-FeOOH Microspheres Produced by a Simple Green Method and Its Outstanding Ability in Heavy Metal Ions Removal. *J. Mater. Chem.* **2011**, *21*, 7878–7881.

43. Wang, B.; Wu, H.; Yu, L.; Xu, R.; Lim, T.-T.; Lou, X. W. Template-free Formation of Uniform Urchin-like α-FeOOH Hollow Spheres with Superior Capability for Water Treatment. *Adv. Mater.* **2012**, *24*, 1111–1116.

44. Boal, A. K.; Headley, T. J.; Tissot, R. G.; Bunker, B. C. Microtunule-Templated Biomimetic Mineralization of Lepidocrocite. *Adv. Funct. Mater.* **2004**, *14*, 19–24.

45. Liang, X.; Wang, X.; Zhuang, J.; Chen, Y.; Wang, D.; Li, Y. Synthesis of Nearly Monodisperse Iron Oxide and Oxyhydroxide Nanocrystals. *Adv. Funct. Mater.* **2006**, *16*, 1805–1813.

46. Jiao, S.; Xu, L.; Hu, K.; Li, J.; Gao, S.; Xu, D. Morphological Control of α-FeOOH Nanostructures by Electrodeposition. *J. Phys. Chem. C* **2010**, *114*, 269–273.

47. Mao, X.; Yang, H.; Zhou, X.; Wang, C.; Wang, Y.; Yang, Y.; Wang, C.; Liu, G. Straight and Branched Goethite Topology by Oriented Attachment at High pH. *Cryst. Growth Des.* **2010**, *10*, 504–509.

48. Wang, B.; Chen, J. S.; Wu, H. B.; Wang, Z.; Lou, X. W. Quasiemulsion-Templated Formation of α-Fe$_2$O$_3$ Hollow Spheres with Enhanced Lithium Storage Properties. *J. Am. Chem. Soc.* **2011**, *133*, 17146–17148.

49. Sudakar, C.; Subbanna, G. N.; Kutty, T. R. N. Synthesis of Acicular Hydrogoethite (α-FeOOH·xH$_2$O; 0.1 < x < 0.22) Particles Using Morphology Controlling Cationic Additives and Magnetic Properties of Maghemite Derived from Hydrogoethite. *J. Mater. Chem.* **2002**, *12*, 107–116.

50. Antony, H.; Peulon, S.; Legrand, L.; Chausse, K. Electrochemical Synthesis of Lepidocrocite Thin Films on Gold Substrate—EQCM, IRRAS, SEM, and XRD Study. *Electrochim. Acta* **2004**, *50*, 1015–1021.

51. Li, J. T.; Zhao, W.; Huang, F. Q.; Manivannan, A.; Wu, N. Q. Single-Crystalline Ni(OH)$_2$ and NiO Nanoplatelet Arrays as Supercapacitor Electrodes. *Nanoscale* **2011**, *3*, 5103–5109.

52. Amano, F.; Li, D.; Ohtani, B. Fabrication and Photo-electrochemical Property of Tungsten(VI) Oxide Films with a Flake-Wall Structure. *Chem. Commun.* **2010**, *46*, 2769–2771.

53. Chen, H. H.; Zou, R. J.; Wang, N.; Chen, H. H.; Zhang, Z. Y.; Sun, Y.; Yu, L.; Tian, Q. W.; Chen, Z. G.; Hu, J. Q. Morphology-Selective Synthesis and Wettability Properties of Well-Aligned Cu$_{2-x}$Se Nanostructures on a Copper Substrate. *J. Mater. Chem.* **2011**, *21*, 3053–3059.

54. Liu, J. P.; Li, Y. Y.; Huang, X. T.; Li, G. Y.; Li, Z. K. Layered Double Hydroxide Nano- and Microstructures Grown Directly on Metal Substrates and Their Calcined Products for Application as Li-Ion Battery Electrodes. *Adv. Funct. Mater.* **2008**, *18*, 1448–1458.

55. Guo, X. X.; Zhang, F. Z.; Xu, S. L.; Evans, D. G.; Duan, X. Preparation of Layered Double Hydroxide Flms with Different Orientations on the Opposite Sides of a Glass

Substrate by *in Situ* Hydrothermal Crystallization. *Chem. Commun.* **2009**, 6836–6838.

56. Pokroy, B.; Kang, S. H.; Mahadevan, L.; Aizenberg, J. Self-Organization of a Mesoscale Bristle into Ordered, Hierarchical Helical Assemblies. *Science* **2009**, *323*, 237–240.

57. Zhang, W. X.; Yang, S. H. *In-Situ* Fabrication of Inorganic Nanowire Arrays Grown from and Aligned on Metal Substrates. *Acc. Chem. Res.* **2009**, *42*, 1617–1627.

58. Geng, F. X.; Zhao, Z. G.; Cong, H. T. Genvironment-Friendly Microemulsion Approach to α-FeOOH Nanorods at Room Temperature. *Mater. Res. Bull.* **2006**, *41*, 2238–2243.

59. Sun, T.; Feng, L.; Gao, X.; Jiang, L. Bioinspired Surfaces with Special Wettability. *Acc. Chem. Res.* **2005**, *38*, 644–652.

60. Feng, L.; Li, S. H.; Li, Y. S.; Li, H. J.; Zhang, L. J.; Zhai, J.; Song, Y. L.; Liu, B. Q.; Jiang, L.; Zhu, D. B. Super-Hydrophobic Surfaces: From Natural to Artificial. *Adv. Mater.* **2002**, *14*, 1857–1860.

61. Jopp, J.; Grüll, H.; Yerushalmi-Rozen, R. Wetting Behavior of Water Droplets on Hydrophobic Microtextures of Comparable Size. *Langmuir* **2004**, *20*, 10015–10019.

62. Lackovic, K.; Angove, M. J.; Wells, J. D.; Johnson, B. B. Modeling the Adsorption of Cd(II) onto Goethite in the Presence of Citric Acid. *J. Colloid Interface Sci.* **2004**, *269*, 37–45.

63. Buerge-Weirich, D.; Hari, R.; Xue, H. B.; Behra, P.; Sigg, L. Adsorption of Cu, Cd, and Ni on Goethite in the Presence of Natural Ground Water Ligands. *Environ. Sci. Technol.* **2002**, *36*, 328–336.

64. Wu, R. C.; Qu, J. H.; Chen, Y. S. Magnetic Powder MnO-Fe_2O_3—A Novel Material for the Removal of Azo-Dye from Water. *Water Res.* **2005**, *39*, 630–638.

65. Deliyanni, E. A.; Matis, K. A. Sorption of Cd Ions onto Akaganeite-Type Nanocrystals. *Sep. Purif. Technol.* **2005**, *45*, 96–102.

66. Gao, Y.; Wahi, R.; Kan, A. T.; Falkner, J. C.; Colvin, V. L.; Tomson, M. B. Adsorption of Cadmium on Anatase Nanoparticles-Effect of Crystal Size and pH. *Langmuir* **2004**, *20*, 9585–9593.

67. Otero, M.; Lopes, C. B.; Coimbra, J.; Ferreira, T. R.; Silva, C. M.; Lin, Z.; Rocha, J.; Pereira, E.; Duarte, A. C. Priority Pollutants (Hg^{2+} and Cd^{2+}) Removal from Water by ETS-4 Titanosilicate. *Desalination* **2009**, *249*, 742–747.